The HPS electromagnetic calorimeter **D R A F T**

I. Balossino[a], N. Baltzell[b], M. Battaglieri[a], E. Buchanan[c], A. Celentano[a], G. Charles[d,*], L. Colaneri[d,e], A. D'Angelo[e], R. DeVita[a], R. Dupré[d], M. Ehrhart[f], M. Garçon[b,g,*], F.-X. Girod[b], M. Guidal[d], M. Holtrop[h], V. Iurasov[d], V. Kubarovsky[b], K. McCarty[h], R. Paremuzyan[h], E. Rauly[d], B. Raydo[b], E. Rindel[d], P. Rosier[d], S. Stepanyan[b], H. Szumila-Vance[f], L. B. Weinstein[f]

[a] *Istituto Nazionale di Fisica Nucleare, Sezione di Genova e Dipartimento di Fisica dell'Universitá, 16146 Genova, Italy*
[b] *Thomas Jefferson National Accelerator Facility, Newport News, Virginia 23606*
[c] *University of Glasgow, Glasgow, G12 8QQ, Scotland, UK*
[d] *Institut de Physique Nucléaire, CNRS/IN2P3, Université Paris-Saclay, Orsay, France*
[e] *Istituto Nazionale di Fisica Nucleare, Sezione di Roma Tor Vergata, 00133 Roma, Italy*
[f] *Old Dominion University, Norfolk, Virginia 23529*
[g] *Irfu/SPhN, CEA, Université Paris-Saclay, 91191 Gif-sur-Yvette, France*
[h] *University of New Hampshire, Department of Physics, Durham, NH 03824*

Abstract

The Heavy Photon Search experiment (HPS) performs a search for a new gauge boson, so-called the "heavy photon". Through its kinetic mixing with the Standard Model photon, this particle would decay into an electron-positron pair. It would then be detectable as a narrow peak in the invariant mass spectrum of such pairs, or, depending on its lifetime, by a decay downstream of the production target. The HPS experiment is installed in Hall-B of Jefferson Lab. This article presents the design and performance of one of the two detectors of the experiment, the electromagnetic calorimeter, during the runs performed in 2015-2016. The calorimeter's main purpose is to provide a fast trigger and reduce the copious background from electromagnetic processes through matching with a tracking detector. The detector is a homogeneous calorimeter, made of 442 lead-tungsten ($PbWO_4$) scintillating crystals, each read-out by an avalanche photodiode coupled to a custom trans-impedance amplifier.

*Corresponding authors:
Email addresses: charlesg@ipno.in2p3.fr (G. Charles), michel.garcon@cea.fr (M. Garçon)

Keywords: heavy photon, dark photon, electromagnetic calorimeter, lead-tungstate crystals, avalanche photodiodes.
2010 MSC: 00-01, 99-00

1. Introduction

The heavy photon, also known as A' or dark photon, is a conjectured massive gauge boson associated with a new U(1) hidden symmetry, and the possible force carrier between dark matter particles. Such a heavy photon has been envisioned by several theories beyond the Standard Model and is also a good candidate to explain some existing astrophysical anomalies. The A' would interact with particles of the hidden sector and kinetically mix with the ordinary photon [1]. This kinetic mixing induces its weak coupling to electrons allowing heavy photons to be radiated in electron scattering and subsequently decay into electron-positron pairs. If the coupling is large enough, they should be observable above the QED background, in the e^+e^- invariant mass spectrum, while if it is small, heavy photons would travel detectable distances before decaying. The HPS experiment is designed to exploit both signatures. Benefitting from the full duty cycle of the electron beam available at Jefferson Lab, several data-taking runs have started and are planned with beam energies between 1 GeV and 6.6 GeV. The electron beam, of intensity between 50 nA and 400 nA, impinges on 0.15% - 0.25% radiation length tungsten foils. A silicon microstrip vertex tracker (SVT) begins 10 cm downstream of the target within the gap of a dipole magnet for the determination of the leptons' momenta and angles, while the electromagnetic calorimeter (ECal) is located 139 cm from the target, outside that magnet, and serves primarily as a fast trigger. Both SVT and ECal are placed as close as possible to the horizontal plane containing the beam, thus allowing the detection of lepton pairs with very small opening angles and a sensitivity to heavy photons in the mass range from 20 MeV/c^2 to 1 GeV/c^2. The experiment is installed in Hall-B at Jefferson Lab, positioned at the downstream end of the

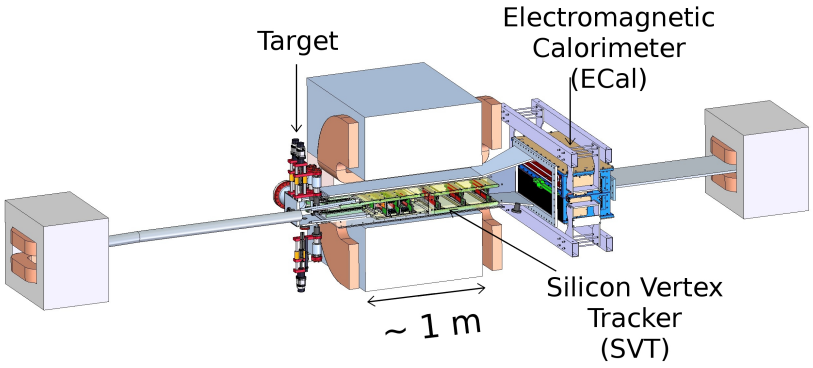

Figure 1: Schematic layout of the HPS experiment: the beam coming from the left is deviated toward the target placed at the entrance of the second analyzing dipole magnet. The SVT is within the gap of this dipole, and ECal right after. The last magnet steers the beam back into the intial direction towards the beam dump.

hall in the configuration illustrated in Fig. 1.

A test run was performed in May 2012 with a partial detector setup, as described in Ref. [2]. We detail here the design and performance of the final calorimeter during the engineering 2015-2016 runs. The paper is organized as follows. We first present the calorimeter design and layout, with special emphasis on the modifications made after the test run. The subsequent Section deals with Monte Carlo simulations of the detector response. The ECal performance, obtained after time and energy calibrations, is discussed in Section 4. Section 5 is devoted to the trigger performance. Section 6 addresses some aspects of SVT track and ECal cluster matching and followed by a summary of the main achievements.

2. Calorimeter description

In order to provide a reliable trigger in a high-background environment (up to 1 MHz/cm^2), the HPS electromagnetic calorimeter must be fast and match the lepton-pair acceptance of the SVT, while operating in the fringe field of the

analyzing dipole. Electrons and positrons between 0.3 GeV and 6.6 GeV are to be measured with an energy resolution of the order of $4\%/\sqrt{E}$ and a position resolution of about 1 to 2 mm to match with the corresponding information coming from the SVT.

For these purposes, a homogeneous calorimeter made of lead tungsten ($PbWO_4$) scintillating crystals was constructed. $PbWO_4$ crystals have a fast decay time ($\approx$ 10 ns) thus allowing to operate in the HPS high-rate environment with a reduced pile-up probability, and a reasonable light yield, compatible with the energy resolution requirements for this experiment. The calorimeter was constructed with crystals originally installed in the inner calorimeter of the CLAS detector [3], after being refurbished. Given the presence of a high magnetic field, avalanche photodiodes were used for light readout, coupled to custom preamplifiers. Major improvements with respect to the test-run configuration include larger area avalanche photodiodes, optimized low-noise preamplifiers, new mother-boards for the routing of high-voltage and signals, and a new light-monitoring system.

2.1. Crystals and ECal lay-out

The calorimeter design is shown in Fig. 2. In order to avoid a vertical 15 mrad zone of excessive electromagnetic background, the ECal is built as two separate halves that are mirror reflections of one another about the horizontal plane of the scattered beam in the dipole field.

Each half is made of 221 modules supported by aluminum frames and arranged in a rectangular formation with five layers of 46 crystals. The two layers closest to the beam have 9 modules removed to allow a larger opening for the outgoing, partially degraded, electron beam and copious Bremstrahlung photons. The layout of a single module is shown in Fig. 3.

Each module is made of a 160-mm long, tapered $PbWO_4$ crystal, with a front (rear) face of 13.3×13.3 mm^2 (16×16 mm^2), wrapped in a VM2002 reflecting foil to increase light collection. The 10×10 mm^2 Hamamatsu photo-sensor [4] is glued on the rear face and connected to the preamplifier [5] held by a connection board that also serves as a thermal screen. The signal is then routed through

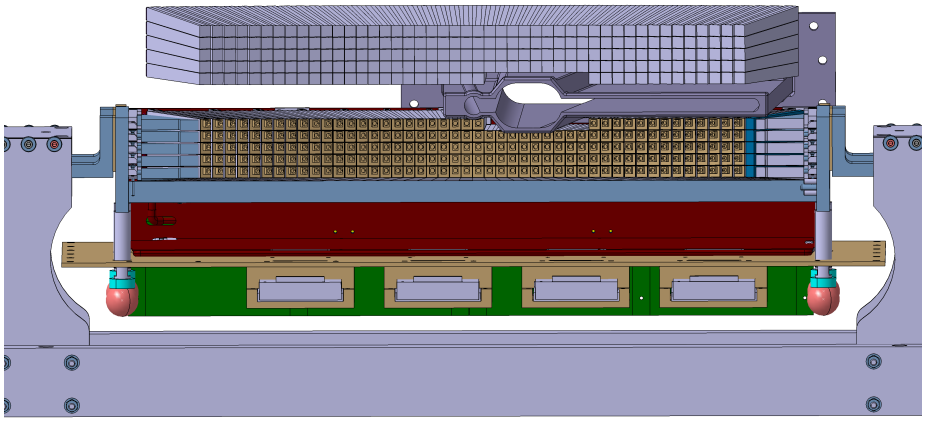

Figure 2: ECal crystal lay-out, as seen in the beam direction. For clarity, the top-half mechanical parts have been removed. For the bottom half, some mechanical elements such as the mother boards (in green) and the copper plates for heat shielding (in red) are visible. Between the two halves of ECal, the beam vacuum vessel is seen to be extended to the right to accommodate for beam particles having lost energy through scattering or radiation.

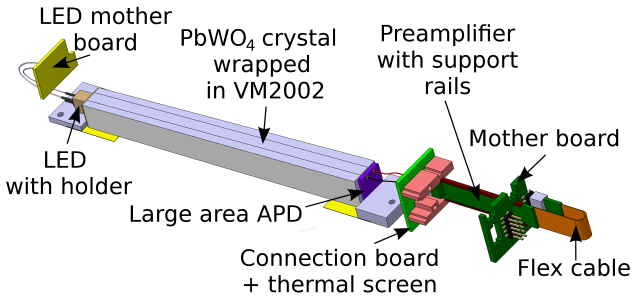

Figure 3: A schematic view of an ECal module.

a mother board to the external DAQ system. On the front face, each crystal hosts a bi-color light-emitting diode (LED) that serves as a monitoring device, as described later.

To stabilize the crystal light yield and the APD gains, each half of the calorimeter is enclosed in a temperature-controlled box. A chiller, operating at

a set value of 17°C, circulates water through these enclosures and maintains a stability better than 0.3°C.

Both halves were held in place by vertical threaded rods attached to rails above the analyzing magnet. The gap between the two halves was determined to be 44 mm, very close to the design value of 40 mm, reproducible to within 0.3 mm after moving them vertically apart in order to perform maintenance work on the SVT, the vacuum system or the ECal itself.

2.2. Light detection and electronics

The major upgrade of the calorimeter system, compared to the 2012 test-run configuration, concerns the introduction of new 10×10 mm^2 Large Area APDs from Hamamatsu. At equivalent deposited energy, about four times more light is collected compared to the 5×5 mm^2 APDs used for the test run. The signal-over-noise ratio is thus increased, allowing for a lower energy threshold and an improved energy resolution.

The dependence of the gain and leakage current on the bias voltage and temperature were measured in a specially designed test bench [6]. A typical result is illustrated in Fig. 4, where the gain is seen to depend on voltage and temperature through a linear combination: $G = G(\alpha V - \beta T)$. After characterizing each photo-sensor, the operating voltage was chosen to yield the best compromise between a high gain and a low dark current. The APDs were then grouped into ensembles of 4 to 10 with similar gain-to-voltage characteristics so that each group could be powered by a single high-voltage channel. The bias voltage of each APD group was selected to insure an average gain of 150 at 18°C for each APD.

The signal from the APD is sent to a preamplifier converting current to voltage and designed to have low input impedance and noise. The gain of the preamplifier was adjusted to ensure that the maximum energy deposition, estimated to be 4 GeV in a single crystal for a beam energy of 6.6 GeV, would not saturate the amplitude converter.

Typical numbers characterizing the whole chain crystal-APD-preamplifier

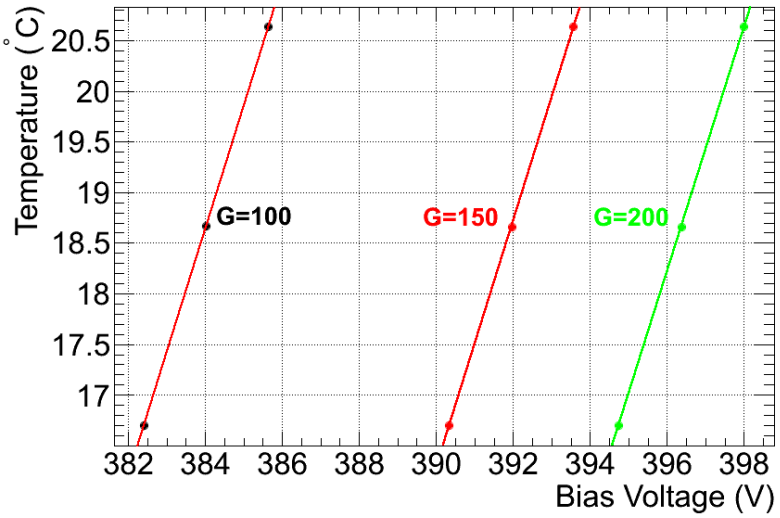

Figure 4: Gain variation with bias voltage and temperature for a typical APD. Circles are interpolations between measurements at fixed temperature and varying voltage. Lines are iso-gain curves in the temperature - bias voltage plane.

are [7]: a light yield of 120 photons (reaching the rear face of the crystal) per MeV of deposited energy, an APD quantum efficiency of 0.7 and gain of 150, a preamplifier gain of 0.62 V/pC (for a 10 ns input pulse width) and a maximal signal amplitude of 2 V. A noise level of a few mV allows thresholds on individual crystals equivalent to 7.5 MeV.

The APD bias voltages (between 385 V and 405 V), the operating voltage of the preamplifiers (±5 V), and their ouput signals are distributed through four circuit boards, known as mother boards. These were completely redesigned after the 2012 test run and careful attention was paid to avoid cross-talk between channels. Each half of the ECal is divided into 26 bias voltage groups. The proper selection of these groups, their matching with the preamplifiers, and the high-voltage fine-tuning, lead to a total gain uniformity on the order of a few percent. Up to fluctuations in the light-yield from crystal to crystal, this provided a good starting point of operation for the trigger set-up.

Finally, for digitization and processing, the signal was sent to a Jefferson

Lab Flash ADC [2, 8] (FADC250) board. The FADC digitizes the APD signal at 250 MHz and stores samples in a 8 μs deep pipeline with 12-bit resolution.

2.3. Slow controls

The slow controls and monitoring of the calorimeter systems are all implemented within the EPICS framework [9]. Graphical interfaces are used for easy user interaction, as well as an alarm system with audible alerts in the control room and automatic email alerts to system experts. Time histories of all slow controls data are preserved and accessed with Jefferson Lab's MYA archiving system [10].

The ECal water cooling is provided by an Anova A-40 chiller operating at 17°C. The internal temperature of the calorimeter is also monitored using sixteen thermocouples located throughout the crystal lattice. The thermocouples are read-out using Omega D5000 series transmitters. Both devices provide RS-232 serial communications.

Low voltage is supplied to the preamplifiers via an Agilent 6221 running at $\pm$ 5 V and 4 A and remotely controlled and monitored from EPICS through a GPIB-ethernet converter.

The serial communications with the Anova and Omega devices are all via a MOXA N-Port 5650 serial to ethernet device server and shielded 50-foot cables between the detector and electronics areas. These are then interfaced with EPICS via its asynchronous driver for controls and monitoring.

Scalers from FADC modules are read into EPICS from a JLab TCP server running on their VXS crates. The current setup provides a graphical display of the 442 scaler channels and a sampling rate of 1 Hz, well below the limits of both hardware and software.

High voltage is supplied to each of the 52 APD groups via CAEN A1520P modules in a SY4527 mainframe. Communications with EPICS is achieved via the manufacturer supplied driver and ethernet connection to the mainframe.

2.4. LED monitoring

Although relatively radiation tolerant, lead-tungstate scintillating crystals are subject to a decrease in light output when exposed to radiation. They recover when the radiation source is removed, through spontaneous thermal-annealing mechanisms (see for example Ref. [11]). In order to preserve the intrinsic energy resolution, the response of the crystals has to be continuously monitored and, if necessary, recalibrated. An LED-based monitoring system was specifically designed and installed in the detector setup after the 2012 test run. Glued on the front face of each crystal, a plastic holder hosts a bi-color LED. These LEDs are connected through twisted-pair wires to four printed-circuit boards which are connected to eight driver circuits, externally mounted on top and bottom of the detector enclosure. A red or blue light pulse with variable amplitude and width can be injected independently in each crystal. By measuring the response of the whole chain (crystal + APD + amplifier) to the pulse, variations in the channel response can be determined and, if necessary, corrected. Furthermore, the radiation damage in the $PbWO_4$ crystals is not uniform over the transmission spectrum as it is mostly concentrated in the blue region (up to $\simeq$ 500 nm). The use of a red/blue bi-color LED can also help in determining which component of the read-out chain is responsible for response variations. During the ECal and trigger commissioning, the LED system was extensively used by turning on one or more channels at a time, sometimes following a programmable pattern.

3. Simulations

A detailed simulation of the electromagnetic showers in the ECal was performed with GEANT4 software to determine the expected detector performances in terms of energy and position resolutions. A main goal of the simulations was to calculate the ratio f of the measured cluster energy E_{rec} to the true (generated) energy E, as a function of the impinging particle type, energy and position. This ratio f will be referred to as "energy correction function" since

it is the correction to be applied to the measured energy in order to recover the true energy. Electrons, positrons and photons were simulated at discrete energies, in steps of 0.1 GeV between 0.3 and 1.1 GeV, in order to uniformly cover the range of energies detectable in the run performed at 1.05 GeV beam energy. The same cluster reconstruction code as the one used for real data was then applied, and the obtained reconstructed energy was compared to the real value to evaluate f. The following thresholds were applied on the measured energy: 7.5 MeV for individual hits (per crystal), 50 MeV for the seed hit in a cluster and 100 MeV for the cluster energy. A seed hit is defined as the crystal with the greatest energy deposition in a given cluster. Results for f are illustrated in Fig. 5 for particles hitting the ECal in the fiducial zone, defined as the area occupied by the inner crystals (that is excluding crystals at the calorimeter edges). The form of the energy correction function is well described by a 3-parameter

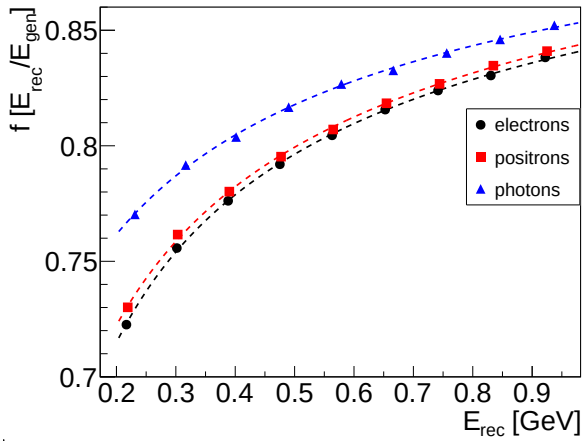

Figure 5: f ratio for electrons, positrons and photons as a function of cluster energy (simulation within a fiducial cut).

fit :

$$f \equiv \frac{E_{rec}}{E} = \frac{A}{E_{rec}} + \frac{B}{\sqrt{E_{rec}}} + C. \quad (1)$$

The incident angle (with respect to the crystal axis) of particles varies with position across the calorimeter. For photons, this is due to the fact that the

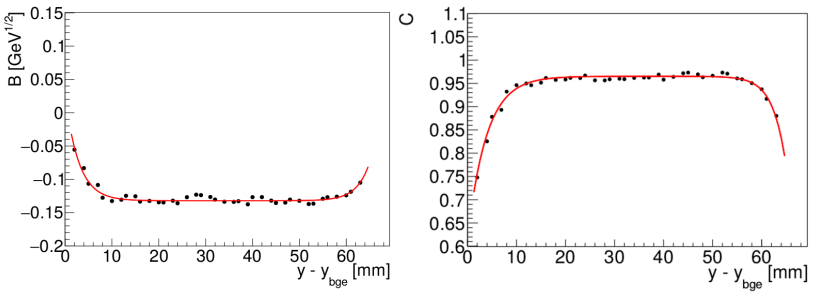

Figure 6: Parameters B and C from Eq 1 for electrons, as a function of vertical position relative to the innermost beam gap edge.

tapered crystals are pointing downstream of the target position. For electrons and positrons, the deflection in the magnetic field induces energy-dependent impact positions and incident angles. These effects are the main cause of the differences between the energy correction functions for the three particle types seen in Fig. 5.

The shower leakage effects in the ECal are more important close to its edges. The correction function f was studied and parameterized as a function of distance to the edge of the calorimeter. It is effectively constant in the central region of the ECal but drops off rapidly in the outermost crystals. In Eq. 1, the parameter A is not significantly correlated with position and remains constant for a given particle type. Moreover, the contribution of A/E is small compared to the two other terms. The parameters B and C are strongly correlated with the position of the cluster relative to the ECal edge. This is illustrated in Fig. 6 for electrons. The true (generated) value is used to determine the position of the particle at the face of the ECal, whereas in data, this position value comes from the SVT tracking. The parameters B and C are fit with two exponential functions at the edges that match in the central region of the ECal. This procedure was refined to take into account the exact geometry around the beam gap, where there are four crystals in each half-column instead of five. Finally, it was extended to the vertical edges with a dependence on the horizontal coor-

dinate. The procedure was repeated for positrons and photons, with the same functional forms but slightly different parameters obtained from the fits.

We point out that these simulations are critical for understanding the electromagnetic shower leakage near the edges of the calorimeter: while the correction function f can be studied with data within the fiducial zone, the full energy correction at the edges is difficult to extract from real data as the energy resolution dramatically deteriorates (see Section 4.2).

The simulation was also used to optimize the determination of the cluster position. The horizontal position x of a cluster was determined by weighting the corresponding crystals centers, x_i, with a proper energy-dependent factor w_i:

$$x = \frac{\sum_i w_i x_i}{\sum_i w_i} + \Delta x, \text{ with } w_i = \max\left[0, w_0 + \ln\frac{E_i}{E_{rec}}\right], \quad (2)$$

and similarly for the vertical position y [12]. The parameter $w_0 = 3.1$ acts as a relative energy threshold $E_i/E_{rec} > e^{-w_0}$, while the logarithmic weights favor the lateral tails of the shower for a more precise position determination. In addition, for the horizontal coordinate only, a linear correction $\Delta x(x)$ is added, due to the angle of incidence of the tracks upon the crystal [13]. This correction depends on the type of particle. These studies showed that the expected resolution on both coordinates is of the order of 2 mm for 1 GeV particles. Considerations on the position using data can be found in Section 6.

4. Calorimeter performance

4.1. Energy calibration

Three physical processes were used to calibrate the ECal energy response. The initial gain calibration was accomplished by measuring the energy deposition from cosmic rays. The gain coefficients were then refined by using elastically-scattered electrons carrying nearly the full beam energy. These two calibration points cover the smallest and the largest energies to be measured by the ECal. Finally, wide-angle Bremsstrahlung events were studied to adjust the simulated correction functions f for mid-range particle energies. We note

that, for optimal energy determination, the energy deposited in each crystal was extracted from a fit to the pulse shape as described in Section 4.3.1.

4.1.1. Calibration with cosmic rays

In order to measure the ECal response of nearly vertical cosmic rays, two plastic scintillator paddles were placed below the detector, triggering the readout of all crystals during periods with no beam on target. Among the tracks collected, only the most vertical ones were kept to minimize the variations of path length across each crystal. This ensured that the energy deposited in the crystal was on average about 18.3 MeV as calculated from simulation. As an example, the signals from a cosmic ray muon passing vertically through 10 crystals of the ECal can be seen in Fig. 7. As seen from this figure, the signals are

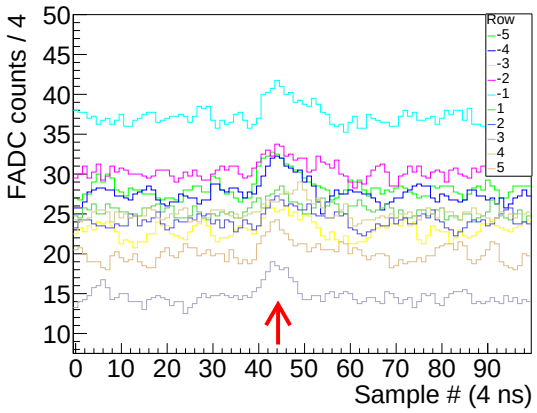

Figure 7: Cosmic ray signal passing vertically through all ten layers of crystals in the ECal. Each crystal's signal is separated vertically in this plot by an offset.

close to threshold, but still usable for an initial calibration. A typical cosmic-ray run lasted approximately 60 hours. The integrated charge distributions from all crystals were then fit to the simulated expectations, and the initial gain calibration was obtained for all 442 channels. The relative energy resolution obtained after this calibration was around $8\%/\sqrt{E(\mathrm{GeV})}$. This method for obtaining the gain value of each channel was sufficient for use in the trigger during runs with

beam (see Section 5).

4.1.2. High-energy calibration with elastically-scattered electrons

Electrons detected in the ECal after small-angle elastic scattering from the target peak nearly at the beam energy. For this calibration, only clusters for which the seed hit carried more than 60% of the full cluster energy were kept. Furthermore, the seed hit energy was required to be larger than 450 MeV during the run at 1.05 GeV beam energy, and larger than 1.1 GeV during the run at 2.3 GeV. A given crystal was calibrated using all clusters for which it is the seed. The high-energy calibration resulted from the comparison of the measured cluster energy with the one expected from simulations. Since the procedure involves using the full cluster energy, thus including information from multiple crystals, it was iterated until all values of individual crystal gains were stable within 1%. After completing two iterations to these corrections, the 366 crystals that had geometric acceptance for elastically-scattered electrons were calibrated. As expected from simulations, due to the combined effect of geometry and magnetic field deflection, elastically-scattered electrons cannot reach several crystals on both right and left sides of the ECal.

The energy correction functions f defined above were then applied to the measured cluster energies. The corrected energy of all elastically-scattered electron clusters is shown in Fig. 8 and used to evaluate the ECal energy resolution as discussed in Sections 4.1.5 and 4.2.

4.1.3. Calibration with wide-angle Bremsstrahlung

The primary physics trigger for two cluster e^+e^- events also recorded a high yield of wide-angle Bremsstrahlung (WAB) events composed of a photon and an electron. These events are selected from two-clusters events, keeping only those with a single matching electron track in the SVT. The sum of energies of these two particles is expected to equal the beam energy. After the calibrations described above, this energy sum was found to be slightly lower, demonstrating that an adjustment of the correction function was needed in the mid-energy

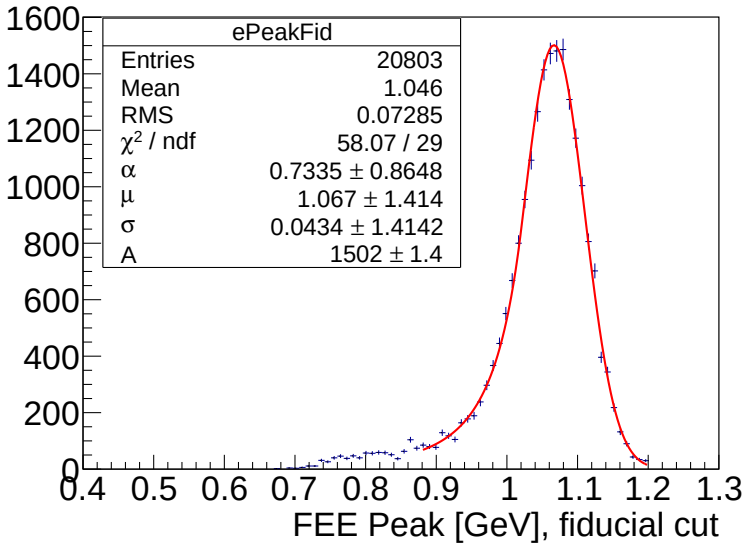

Figure 8: Measured energy of elastically-scattered electrons after calibration and correction f due to shower leakage, at a beam energy of 1.05 GeV. This plot sums over all seed hit crystals except those on a calorimeter edge. The spectrum is fit with a Crystal Ball Function, see [14] for details.

range.

For each WAB event, the energy sum of the two corrected clusters was calculated as :

$$E_{sum} \equiv \frac{E_{e^-}}{f_{e^-}} + \frac{E_\gamma}{f_\gamma} \tag{3}$$

where E_i and f_i are respectively the cluster energy and the shower leakage correction for the electron or the photon. Using Eq. 3, the correction functions f_i were adjusted for each particle such that the sum of the two corrected clusters matches the incident beam energy. It was also required that the ratio f_{e^-}/f_γ be unchanged with respect to the simulation and that the elastically-scattered electrons were not affected. These changes to the energy correction functions were found to be within 1%.

4.1.4. Gain stability

The gain stability was regularly checked during the runs by comparing amplitudes obtained with LEDs over time. The response of each channel to LED pulses with a pre-determined amplitude was measured and compared with a reference value. In preparation, LED settings were equalized to produce a uniform output signal with an amplitude much larger than the channel noise. The LED signals were checked to be stable to better than 1% over periods of 3 days without beam. Figure 9 shows the ratio of LED signal after 70 hours of data taking with beam on target at the nominal luminosity. Most of the crystal gains were stable to within 1%. Around the vacuum vessel, where the particle rate was much higher, the gains are slightly reduced.

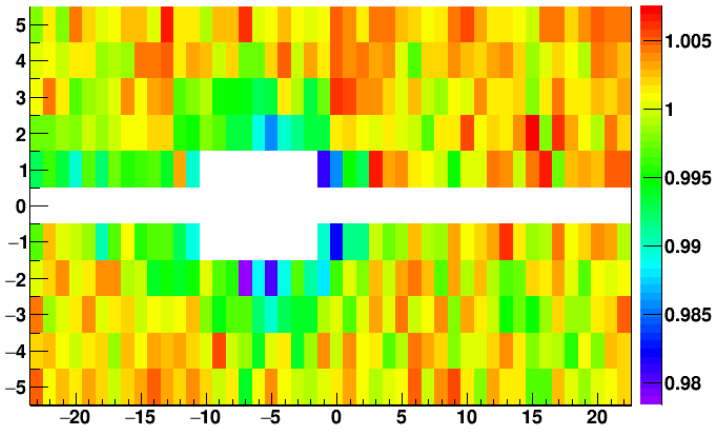

Figure 9: Signal ratio from the LED, as given by the color scale on the right, after 70 hours of data taking: LED amplitude after data taking over initial amplitude. The axes tick labels refer to the crystals' numbering scheme, ECal being viewed from downstream.

4.1.5. Energy resolution in the fiducial region

The calibration with elastically-scattered electrons provided the cleanest point in understanding the energy resolution at the beam energy. WAB events were used to assess the energy resolution at lower energies. By very tightly

cutting on the energy of the photons, the energy resolution of electrons could be studied both as a function of energy and position relative to the edges of the ECal. The resulting energy resolution is shown in Fig. 10.

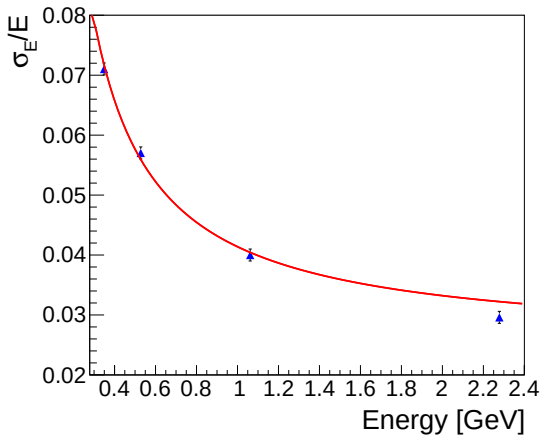

Figure 10: Energy resolution in the ECal as found in data by using elastically-scattered electrons and WAB events. The fit is given by Eq. 4. It was performed using only data at 1.05 GeV beam energy.

The fit to the energy resolution results in:

$$\frac{\sigma_E}{E}(\%) = \frac{1.62}{E} \oplus \frac{2.87}{\sqrt{E}} \oplus 2.5, \tag{4}$$

where the $\oplus$ symbol indicates a quadratic sum and E is in units of GeV. In Eq. 4, the first term is generally attributed to electronic noise. The second term is related to the statistical fluctuations of the shower containment and the APD gain. The last term contains both the energy leakage out the back of the ECal and the crystal-to-crystal inter-calibration error.

4.2. Edge effects

To understand the resolution as close as possible to the edges of the calorimeter, a specific study was performed using events from both WAB and elastically-scattered electrons. The electron position at the ECal, given by the SVT track, was used to determine the electron's distance from the beam gap edge. In the

case of WAB events, the photon was required to be within the ECal fiducial region.

A mid-energy point at approximately 0.5 GeV was obtained by selecting WAB events where the energy difference between the two particles was less than 100 MeV. When selecting only events where both particles are in the fiducial region, the energy resolution can be assumed to be the same for both particles and is readily obtained by dividing the standard deviation of the energy sum peak by $\sqrt{2}$. Once this resolution was extracted, the dependence on the electron vertical position could be obtained from the data by relaxing the condition on this particle to be in the fiducial region (see Fig. 11):

$$\sigma_{E_{e^-}}(y) = \sqrt{\sigma^2_{E_{e^-}+E_\gamma}(y) - \sigma^2_{E_{e^-}+E_\gamma}(y_0)/2}, \tag{5}$$

where y_0 is in the middle of the fiducial region.

A similar procedure was used to find the resolution for highly energy-asymmetric clusters, selecting 0.7 GeV photons in the fiducial region to study the resolution for 0.35 GeV electrons as a function of position. Combining the analysis of elastically-scattered electrons, the resolution as a function of position was then obtained for three energies (about 0.35, 0.5 and 1.05 GeV). It was found that the second parameter of the energy resolution function, $b/\sqrt{E}$, is the most strongly correlated with the position in the ECal. By fixing the other two parameters to the values in the fiducial region (see Eq. 4), the b parameter was determined as a function of position, as illustrated in Fig. 12. The ECal energy resolution dependence on both the energy and vertical position is simply given by:

$$\frac{\sigma_E}{E}(\%) = \frac{1.62}{E} \oplus \frac{b(y - y_{bge})}{\sqrt{E}} \oplus 2.5 \tag{6}$$

where, y_{bge} is the y position at the inner gap edge. Similarly to previous such fits at the edges, two matching exponentials were used to parameterize b:

$b(|y - y_{bge}| < p_0) = p_1 - p_2 e^{-(y-p_3)\cdot p_4}$,

$b(|y - y_{bge}| > p_0) = p_1 - p_5 e^{-(y-p_6)\cdot p_7}$.

The energy resolution deteriorates rapidly within 8-10 mm from the edge of the calorimeter. Equation 6 is however reliable down to 6.5 mm (which corresponds

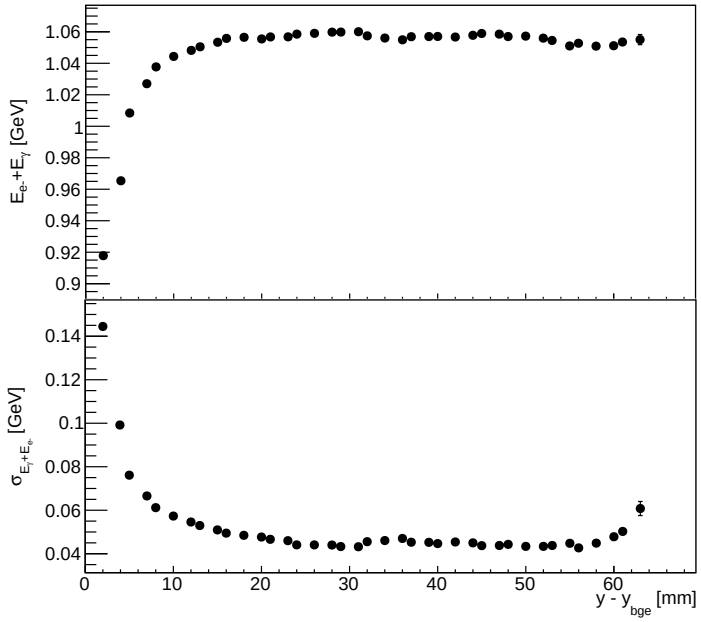

Figure 11: WAB events with $|E_{e^-} - E_\gamma| < 0.1$ GeV. Top: energy sum ($E_{e^-} + E_\gamma$) peak position. Bottom: energy sum peak standard deviation $\sigma_{E_{e^-}+E_\gamma}(y)$ as a function of vertical position of the electron across the ECal.

to the center of the last crystal front face) from the edge of the calorimeter.

4.3. Time calibration

HPS is a high rate experiment, up to 1 MHz per crystal and 30 MHz for the whole calorimeter, with a 15 MeV threshold and for typical run conditions. The time calibration is thus a key element for reducing backgrounds for accidentals and measuring well correlated two cluster events.

4.3.1. Crystal pulse fitting

The time of a cluster is set from the seed crystal (the highest energy in the cluster). This crystal pulse shape, sampled at 250 MHz by the FADC, is fit by the sum of a pedestal P and a 3-pole function with width τ and time t_0 [7]:

$$\mathrm{ADC}(t) = P + \frac{A}{2\tau^2}\,(t - t_0)^2\, e^{-(t-t_0)/\tau} \tag{7}$$

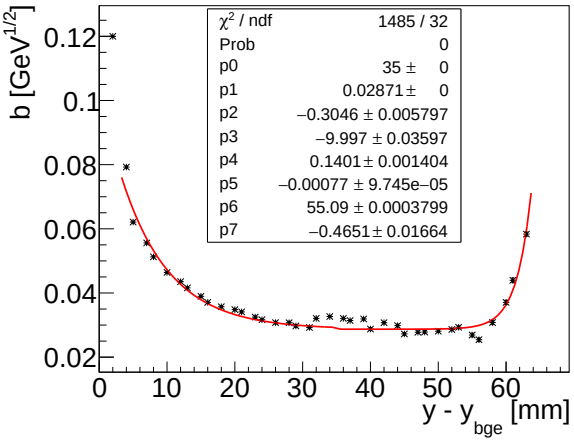

Figure 12: The stochastic parameter (corresponding to $1/\sqrt{E}$ term) of the energy resolution description as a function of vertical position relative to the ECal beam gap edge. The fit function is given Eq. 6.

An example fit is shown in Fig. 13. Best resolutions were obtained by fixing, for each crystal independently, the width parameter to the average value measured over many pulses [15].

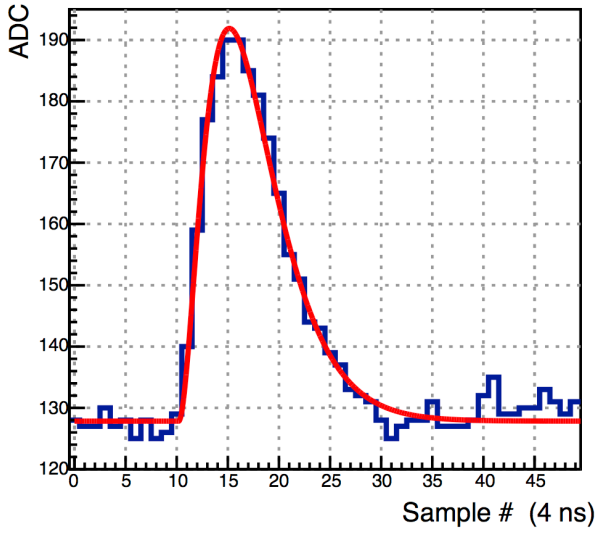

Figure 13: Example fit of an individual crystal pulse.

4.3.2. Crystal time alignment

Corrections to the above defined pulse time t_0 are needed in order to align all crystals in time:

$$t = t_0 + \Delta t_{RF} + \Delta t_{tw}(E), \tag{8}$$

where $\Delta t_{tw}(E)$ is the time walk correction and Δt_{RF} the time offset obtained before time walk corrections. The two quantities are discussed successively hereafter.

The accelerator 499 MHz RF signal, measured with a FADC channel in the exact same conditions as the ECal signals, is sampled in one of every 80 bunches. The precision at which this signal is measured has been determined to be 24 ps. Because of this sampling, the time difference between the RF signal and a crystal exhibits peaks spaced by 2.004 ns (see Fig. 14). Using the modulo of the time difference of the hit time with RF signal time, one can achieve a common centering of these peak patterns for all crystals with a fine offset smaller than 2.004 ns.

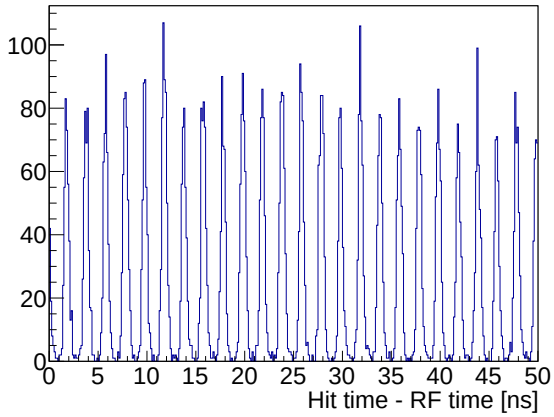

Figure 14: Time difference between a single crystal hit and the RF time.

After aligning all crystal time signals in increments of 2.004 ns, the time difference between two clusters is used. For these events, correlated clusters are

required to have an energy sum close to the beam energy, an energy difference less than 200 MeV, and occur within a given trigger time window. The time difference between the two seed crystals is recorded for each of these. This procedure is repeated for many events. The resulting distributions are characterized by the 2.004 ns interval pattern as seen in Fig. 15. The time of the largest peak indicates the offset in increments of 2.004 ns that should be applied in addition to the previous offset to obtain Δt_{RF}.

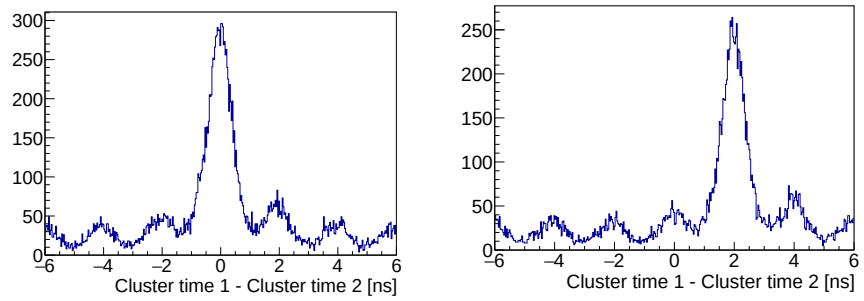

Figure 15: Time difference between the seed hits of two correlated clusters after RF calibration. Cluster 1 has a given (fixed over all events) seed crystal while cluster 2 may be anywhere in ECal. The left and right plots show events for two different choices of seed crystals for cluster 1.

In order to determine the energy dependence of the time offsets, or time walk, the time differences between individual hits in a cluster and the highest energy hit were studied as a function of hit energy. The results are fitted by an exponential and a second order polynomial, as shown in Fig. 16, and form the basis of a time-walk correction. The time walk is very small for crystal energies above 150 MeV, and thus does not significantly affect the resolution of the two-cluster time difference. It is however important for the time offsets in the clustering algorithm in order to enable tighter time cuts between crystals.

4.3.3. Time resolution

Finally, the time resolution as a function of hit energy is extracted from the width of the time coincidences within single clusters. The result is shown in

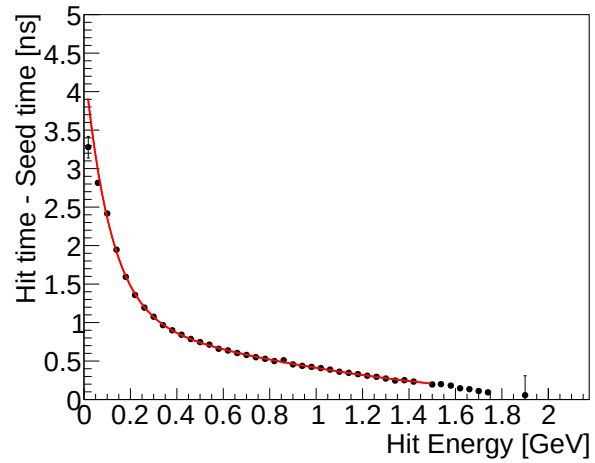

Figure 16: Time walk correction as a function of hit energy (within clusters where the seed hit energy is greater than 400 MeV).

Fig. 17, and the time resolution can be parameterized as [16]:

$$\text{Time resolution (ns)} = \frac{0.188}{E\ (\text{GeV})} \oplus 0.152. \tag{9}$$

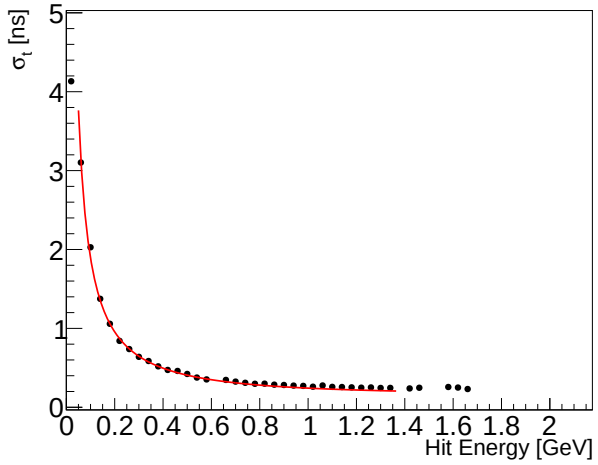

Figure 17: Individual crystal time resolution as a function of energy.

The obtained time resolution is significantly smaller than the intrinsic 4 ns

FADC sampling period and enables the use of the ECal to improve offline event selection and reduce accidentals from the final analysis.

5. Trigger performance

The electromagnetic calorimeter is the only detector used in the HPS trigger decision. Therefore a significant effort has been made to ensure that it has an efficient background rejection while maximizing the acceptance for A' events.

5.1. General scheme of the trigger

The HPS trigger scheme is as follows. The analog signal from each ECal channel is continuously sampled by the FADC every 4 ns. When the signal crosses a selectable threshold, N_1 samples before crossing and N_2 samples after (typically 5 and 25) are summed together to provide the pulse charge, which is then converted to energy, using online gains and pedestals loaded, channel by channel, in the FADC. The resulting energy and threshold crossing time are then passed every 16 ns to the clustering algorithm in the General Trigger Processor board (GTP).

The first step of processing in the GTP is finding seed crystals. A hit is considered to be a seed if it fulfills two conditions: an energy higher than a selectable threshold and higher than all its 8 nearest neighbors (or fewer neighbors if it belongs to one of the calorimeter edges).

When one of the crystal energies meets the definition of a seed hit, a time coincidence between the seed hit and its neighbors is then required to group additional hits into the cluster. The timing coincidence is programmable, typically 4 samples, and required to compensate for time-walk effects. The cluster energy is the sum of all the crystal energies within a 3×3 spatial array and time constraints. Once the clustering algorithm on the GTP has identified a cluster, the corresponding data is reported to the main trigger processor. This includes: the timestamp, the energy, and the spatial coordinates (center of the seed crystal). The cluster energy is not corrected for shower leakage effects at this stage.

Finally, the trigger processor makes the trigger decision by applying further selection to the clusters. Currently, two event topologies are considered, with one or two clusters. Parallel trigger selections are implemented in the trigger processor, with an associated prescale factor of $2^{n-1}+1$, where n is selectable.

5.2. Trigger parameters

The system includes two pair triggers, two single cluster triggers, a random pulser trigger for background studies and a calibration trigger for cosmics and the LED monitoring system. All these triggers have separate trigger cuts and can operate simultaneously with individual prescale factors.

The single cluster triggers are based on a lower and upper energy limits and a number of hits in the cluster. One of the single cluster triggers was tuned to select the elastic scattering of electrons off the nuclear target. The second did not have stringent cuts and serves for testing purposes, in particular for the determination of trigger efficiencies.

The two cluster pairs triggers were optimized for different physical processes, and used different sets of parameters. The Pair-0 trigger algorithm was used for the selection of Møller scattering, while Pair-1 was the main trigger for the Heavy Photon search. Each trigger, except Pair-1, has an associated prescale factor, in order to keep the total trigger rate acceptable for the data acquisition system.

The cuts applied for the main trigger, cluster pairs, are presented below. Cluster pairs are generated by forming all possible combinations of clusters from the top and the bottom half of the calorimeter. There are seven cluster-pair cuts. Denoting cluster energy, number of hits, time, and coordinates as E_i, N_i, t_i, x_i, y_i, where $i = 1$ or 2, the cuts are defined as:

$$E_{\text{min}} \leq E_i \leq E_{\text{max}}, \tag{10}$$

$$E_{\text{sum min}} \leq E_1 + E_2 \leq E_{\text{sum max}}, \tag{11}$$

$$N_i \geq N_{\text{threshold}}, \tag{12}$$

$$E_2 - E_1 \leq E_{\text{difference}}, \tag{13}$$

$$E_1 + r_1 F \geq E_{\text{slope}}, \tag{14}$$

$$|\arctan\frac{x_1}{y_1} - \arctan\frac{x_2}{y_2}| \leq \theta_{\text{coplanarity}}, \tag{15}$$

$$|t_1 - t_2| \leq t_{\text{coincidence}}. \tag{16}$$

E_{min}, E_{max}, $E_{\text{sum min}}$, $E_{\text{sum max}}$, $E_{\text{difference}}$, E_{slope}, F, $\theta_{\text{coplanarity}}$, $N_{\text{threshold}}$ and $t_{\text{coincidence}}$ are programmable trigger parameters. E_1 is the energy of the cluster with the lowest energy and $r_1 = \sqrt{x_1^2 + y_1^2}$ is the distance between its center and the calorimeter center.

The values chosen for each parameter were based on Monte Carlo simulations and are summarized in Table 1. The parameters for Pair-1 trigger were tuned for each beam energy and chosen to ensure the best A' signal efficiency and signal-over-background ratio. Figure 18 shows a real event selected by the HPS pair trigger algorithm.

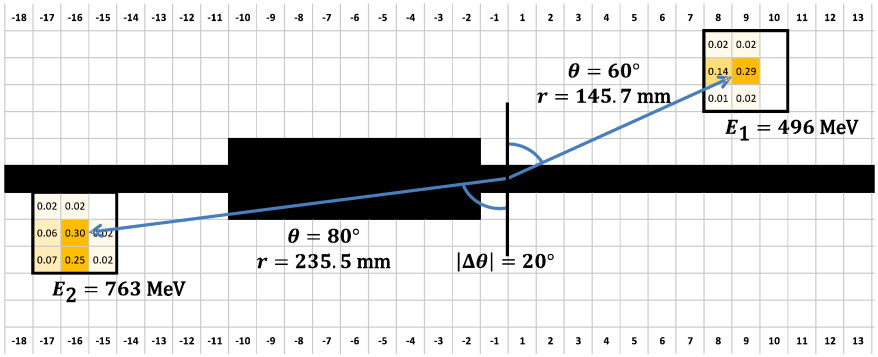

Figure 18: Real event selected by the HPS trigger. The event includes two clusters with energies $E_1 = 496$ MeV at the top part of the calorimeter and $E_2 = 763$ MeV at the bottom half. The corresponding 3×3 spatial windows are shown. The distances r_i between seed crystals and center of the calorimeter are indicated. The coplanarity angle is calculated as $|\theta_1 - \theta_2| = 80° - 60° = 20°$.

Parameter	Single-0	Single-1	Pair-0	Pair-1
E_{min}	0.100 GeV	1.300 GeV	0.150 GeV	0.150 GeV
E_{max}	2.700 GeV	2.600 GeV	1.400 GeV	1.400 GeV
$N_{\text{threshold}}$	3 hits	3 hits	2 hits	2 hits
$E_{\text{sum min}}$	—	—	0.500 GeV	0.600 GeV
$E_{\text{sum max}}$	—	—	1.900 GeV	2.000 GeV
$E_{\text{difference}}$	—	—	1.100 GeV	1.100 GeV
E_{slope}	—	—	0.400 GeV	0.600 GeV
F	—	—	0.0055 GeV/mm	0.0055 GeV/mm
$\theta_{\text{coplanarity}}$	—	—	—	40°
$t_{\text{coincidence}}$	—	—	8 ns	12 ns
Prescale	$2^{12}+1$	$2^{10}+1$	$2^{5}+1$	1

Table 1: All trigger settings for the Single-0, Single-1, Pair-0 and Pair-1 triggers for the run with beam energy 2.3 GeV. Note that energies are not corrected for shower leakage at the trigger stage. The purpose of the different triggers is described in the text.

5.3. Trigger diagnostics

The main diagnostic consists of a comparison between the hardware trigger algorithm and its software simulation. The numbers of clusters and triggers are compared with both the hardware and the simulated triggers. The results show an agreement above 99%. The small difference is due to fluctuations for near-threshold energy in the selection of the clusters and for events at the edge of the time window.

6. Cluster-Track matching

6.1. Need for cluster-track matching

As described in Section 4.1, cluster energy and position corrections depend on particle type. Therefore, it is necessary to know whether each cluster is associated with e^-, e^+, or photon before applying the corrections. This can be determined based on matching the clusters with tracks, or, in the case of

photons, the lack of an associated track. As explained later in this Section, the cluster-track matching also reduces the background.

Tracks reconstructed with the SVT can be extrapolated to the calorimeter to determine their intersection with the ECal. The residual between reconstructed cluster and extrapolated track coordinates is used as a measure of cluster-track matching.

6.2. Selection of samples and determination/parametrization of matching functions

To develop the matching criteria, a strict event selection was applied. Two time-coincident clusters in the ECal and two oppositely charge tracks in the SVT, one in each half of the detector, were required.

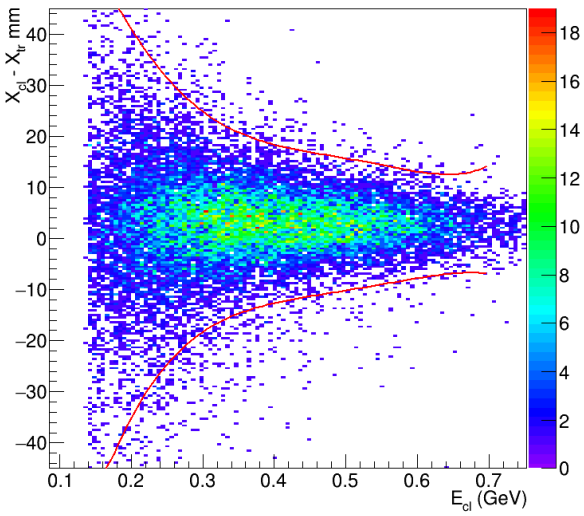

Figure 19: Difference of cluster and track horizontal coordinate (x) as a function of uncorrected cluster energy, for ECal bottom half and negative tracks. Red lines represent our parameterizations of $\mu \pm 3\sigma$.

Due to the possibility of small misalignments of the detector and of the dipole magnet, there can be independent systematic shifts for the two detector halves and particle charges. Therefore the cluster-track matching is studied separately

for all combinations of bottom-top and negative-positive tracks. Since cluster and extrapolated track position resolutions are energy dependent, it is also natural to parametrize the matching as a function of energy.

Figure 19 shows an example of the horizontal coordinate difference between clusters and negative tracks as a function of the uncorrected cluster energy in the bottom half of the detector. This figure also illustrates that this selection is essentially free of background.

In total, there are eight similar distributions: 2 (coordinate) $\times$ 2 (detector half) $\times$ 2 (track charge). All eight were divided into 20 slices of energy, and, for each slice the residuals were fit with a Gaussian function. The Gaussian means μ and widths σ were then parameterized with a 5^{th} degree polynomial as a function of energy. The red lines in Figure 19 show an example of these $\mu \pm 3\sigma$ functions.

To quantify the degree of matching for a particular cluster and track with measured x and y positions, we define a quantity n_σ as

$$n_\sigma = \sqrt{n_{\sigma_x}^2 + n_{\sigma_y}^2}, \tag{17}$$

where

$$n_{\sigma_x} = \frac{x_{cluster} - x_{track} - \mu_x}{\sigma_x}, \tag{18}$$

and similarly for the y-coordinate.

With this matching estimator n_σ defined, we studied its distribution for all combinations of good tracks and clusters in the same detector half (shown in Fig. 20). It can be seen that good matching between tracks and clusters was achieved with small background. Moreover, the matching between the SVT and the ECal allowed the rejection of about 9% of negative tracks for which no match was found ($n_\sigma > 5$) and about 3% of positive tracks.

7. Summary

With all 442 channels and all hardware components fully operational, the HPS electromagnetic calorimeter operated successfully during the first runs of

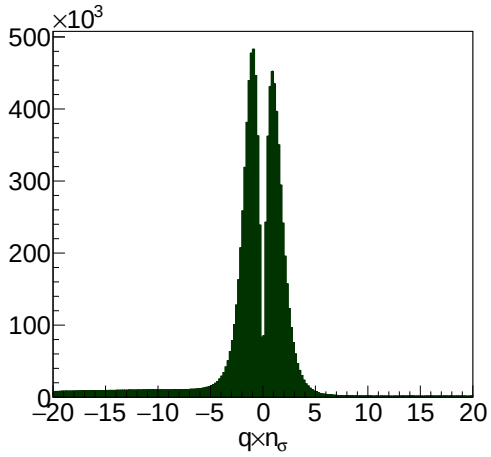

Figure 20: Distribution of $q \times n_\sigma$ for in-time clusters, where q is the electric charge. Positive tracks were weighted by ≈ 6 to have visually the same level as negatives.

the experiment in 2015-2016. Its primary goal of providing a fast trigger in a large background environment was achieved, with online cluster construction and efficient cluster pair selection at a rate of up 30 kHz with only 10% dead time. In addition, detailed simulations and careful calibrations lead to energy and position resolutions about 4% and 2 mm for 1 GeV electrons. The analyses of the data taken at 1.05 GeV and 2.3 GeV beam energies are in progress. The data presented in this paper was collected during engineering runs of 2015 and 2016, the physics runs are planned in the coming years at energies ranging from 1 GeV to 6.6 GeV to cover the planned search domain of the HPS experiment.

Acknowledgements

The ECal could not have been designed and built without the participation of the skilled technical staff at IPNO (Orsay), INFN (Genova and Roma) and Jefferson Lab. The whole HPS collaboration participated in its commissioning and operation during the runs, and numerous discussions within the collaboration helped to refine the analyses described in this article. The Jefferson Lab accelerator crew is thanked for delivering a well tuned beam extremely

close to our detection system. This work was partly supported by a grant from the French National Research Agency (ANR-13-JS05-0001), by a Sesame project HPS@JLab funded by the French region Ile-de-France, by... One of us (M. Garçon) acknowledges support from Jefferson Lab during the assembly and commissioning of ECal

References

[1] R. Essig, J. A. Jaros, W. Wester et al., Planning the future of U.S. Particle Physics, The Intensity Frontier, Dark Sectors and New, Light, Weakly Coupled Particles, arXiv:1311.0029, and references therein.

[2] M. Battaglieri et al., The Heavy Photon Search Test Detector, Nucl. Instrum. Meth. A **777** (2014) 91-101.

[3] F.-X. Girod, Diffusion Compton profondément virtuelle avec le détecteur CLAS pour une étude des distributions de partons généralisées, PhD thesis, Université de Strasbourg (2006), and references therein.

[4] Hamamatsu Si APD S8664-1010.

[5] E. Rauly and G. Charles, Current sensitive preamplifier used for HPS calorimeter, HPS-Note 2016-001.

[6] A. Celentano et al., Design and realization of a facility for the characterization of Silicon Avalanche PhotoDiodes, JINST 9 (2014) T09002, arXiv:1504.01589.

[7] A. Celentano and G. Charles, Characterization of the ECal crystals light yield and amplification chain, HPS-Note 2014-002.

[8] H. Dong et al., Integrated Tests of a High Speed VXS Switch Card and 250 MSPS Flash ADCs (2007).

[9] L.R. Dalesio et al., EPICS Architecture (1991).

[10] C.J. Slominski, A MySQL Based EPICS Archiver, Proc. 12th Int. Conf. on Accelerator and Large Experimental Physics Control Systems, Kobe, Japan (2009).

[11] V.A. Batarin et al., Correlation of beam electron and LED signal losses under irradiation and long-term recovery of lead tungstate crystals, Nucl. Instrum. Meth. A **550** (2005) 543-550.

[12] T. C. Awes et al., A Simple Method of Shower Localization and Identification in Laterally Segmented Calorimeters, Nucl. Instrum. Meth. A **311** (1992) 130.

[13] H. Szumila-Vance and M. Garçon , HPS/ECal simulations: energy and position reconstruction for electrons, positrons and photons, HPS-Note 2014-001.

[14] H. Szumila-Vance, HPS Ecal Energy Calibration for the Spring 2015 Engineering Run, HPS-Note 2016-002.

[15] N. Baltzell, ECal pulse fitting, HPS-Note 2015-010.

[16] H. Szumila-Vance, ECal Timing Calibration for the Spring 2015 Engineering Run, HPS-Note 2015-011